Atom chips in the real world: the effects of wire corrugation

Thorsten Schumm, Jèrôme Estève, Christine Aussibal, Cristina Figl, Jean-Baptiste Trebbia, Hai Nguyen, Dominique Mailly, Isabelle Bouchoule, Christoph I Westbrook, Alain Aspect

EPJ manuscript No.
(will be inserted by the editor)

Atom chips in the real world: the effects of wire corrugation

T. Schumm[1], J. Estève[1], C. Figl[1a], J.-B. Trebbia[1], C. Aussibal[1], H. Nguyen[1], D. Mailly[2], I. Bouchoule[1], C. I. Westbrook[1] and A. Aspect[1]

[1] Laboratoire Charles Fabry de l'Institut d'Optique, UMR 8501 du CNRS, 91403 Orsay Cedex, France
[2] Laboratoire de Photonique et de Nanostructures, UPR 20 du CNRS, 91460 Marcoussis, France

the date of receipt and acceptance should be inserted later

Abstract. We present a detailed model describing the effects of wire corrugation on the trapping potential experienced by a cloud of atoms above a current carrying micro wire. We calculate the distortion of the current distribution due to corrugation and then derive the corresponding roughness in the magnetic field above the wire. Scaling laws are derived for the roughness as a function of height above a ribbon shaped wire. We also present experimental data on micro wire traps using cold atoms which complement some previously published measurements and which demonstrate that wire corrugation can satisfactorily explain our observations of atom cloud fragmentation above electroplated gold wires. Finally, we present measurements of the corrugation of new wires fabricated by electron beam lithography and evaporation of gold. These wires appear to be substantially smoother than electroplated wires.

PACS. 39.25.+k Atom manipulation (scanning probe microscopy, laser cooling, etc.) – 03.75.Be Atom and neutron optics

1 Introduction

Magnetic traps created by current carrying micro wires have proven to be a powerful alternative to standard trapping schemes in experiments with cold atoms and Bose-Einstein condensates [1,2,3,4,5,6,7]. These so-called "atom chips" combine robustness, simplicity and low power consumption with strong confinement and high flexibility in the design of the trapping geometry. Integrated atom optics elements such as waveguides and atom interferometers have been proposed [8] and could possibly be integrated on a single chip using fabrication techniques known from microelectronics. Quantum information processing with a single atom in a micro trap has also been proposed [9].

Real world limitations of atom chip performance are thus of great interest. Losses and heating of atoms due to thermally exited currents inside conducting materials composing the chip were predicted theoretically [10,11] and observed experimentally soon after the first experimental realizations of atomic micro traps [12,13].

An unexpected problem in the use of atom chips was the observation of a fragmentation of cold atomic clouds in magnetic micro traps [14,5]. Experiments have shown that this fragmentation is due to a time independent roughness in the magnetic trapping potential created by a distortion of the current flow inside the micro wire [15]. It has also been demonstrated that the amplitude of this roughness increases as the trap center is moved closer to the micro wire [16]. Fragmentation has been observed on atom chips built by different micro fabrication processes using gold [17] and copper wires [14,5], and on more macroscopic systems based on cylindrical copper wires covered with aluminum [16] and micro machined silver foil [18]. The origin of the current distortion inside the wires causing the potential roughness is still not known for every system.

In a recent letter [17], we experimentally demonstrated that wire edge corrugation explains the observed potential roughness (as theoretically proposed in [19]) in at least one particular realization of a micro trap. In this paper, we will expand on our previous work giving a more detailed description of the necessary calculations as well as presenting a more complete set of experimental observations. We emphasize that extreme care has to be taken when fabricating atom chips, and that high quality measurements are necessary to evaluate their flatness in the frequency range of interest. We will discuss the influence of corrugations both on the edges as well as on the surface of the wire and give scaling laws for the important geometrical quantities like atom wire separation and wire dimensions. We will also present preliminary measurements on wires using improved fabrication techniques.

The paper is organized as follows. In section 2, we give a brief introduction to magnetic wire traps and emphasize that the potential roughness is created by a spatially fluctuating magnetic field component parallel to the wire. In section 3, we give a general framework to calculate the

[a] *Present address: Universität Hannover, D 30167 Hannover, Germany*

rough potential created by any current distortion in the wire. A detailed calculation of the current flow distortion due to edge and surface corrugations on a rectangular wire is presented in section 4. In section 5, we apply these calculations to the geometry of a flat wire, widely used in experiments. Edge and surface effects are compared for different heights above the wire and we present important scaling laws that determine the optimal wire size for a given fabrication quality. In section 6 and 7, we show measurements of the spectra of edge and surface fluctuations for two types of wires produced by different micro fabrication methods: optical lithography followed by gold electroplating and direct electron beam lithography followed by gold evaporation. We also present measurements of the rough potential created by a wire of the first type using cold trapped Rubidium atoms.

2 Magnetic micro traps

The building block of atom chip setups is the so-called side wire guide [8]. The magnetic field created by a straight current carrying conductor along the z axis combined with an homogeneous bias field B_0 perpendicular to the wire creates a two-dimensional trapping potential along the wire (see figure (1)). The total magnetic field cancels on a line located at a distance x from the wire and atoms in a low field seeking state are trapped around this minimum. For an infinitely long and thin wire, the trap is located at a distance $x = \mu_0 I/(2\pi B_0)$. To first order, the magnetic field is a linear quadrupole around its minimum. If the atomic spin follows adiabatically the direction of the magnetic field, the magnetic potential seen by the atoms is proportional to the magnitude of the magnetic field. Consequently, the potential of the side wire guide grows linearly from zero with a gradient B_0/x as the distance from the position of the minimum increases.

For a straight wire along z, all magnetic field vectors are in the (x, y) plane. Three dimensional trapping can be obtained by adding a spatially varying magnetic field component B_z along the wire. This can be done by bending the wire, so that a magnetic field component along the central part of the wire is created using the same current. Alternatively, separate chip wires or even macroscopic coils can be used to provide trapping in the third dimension.

For a realistic description of the potential created by a micro wire, its finite size has to be taken into account. Because of finite size effects, the magnetic field does not diverge but reaches a finite value at the wire surface. For a square shaped wire of height and width a carrying a current I, the magnetic field saturates at a value proportional to I/a, the gradient reaches a value proportional to I/a^2. Assuming a simple model of heat dissipation, where one of the wire surfaces is in contact with a heat reservoir at constant temperature, one finds the maximal applicable current to be proportional to $a^{3/2}$ [20]. Therefore, the maximal gradient that can be achieved is proportional to $1/\sqrt{a}$. This shows that bringing atoms closer to smaller wires carrying smaller currents still increases the magnetic confinement, which is the main motivation for miniaturizing the trapping structures. However the magnetic field roughness arising from inhomogeneities in the current density inside the wire also increases as atoms get closer to the wire. This increase of potential roughness may prevent the achievement of high confinement since the trap may become too corrugated.

Before turning to the calculations of the rough magnetic field, we emphasize that only the z component of the magnetic field is relevant to the potential roughness. A variation of the magnetic field in the (x, y) plane will cause a negligible displacement of the trap center, whereas a varying magnetic field component B_z modifies the longitudinal trapping potential, creating local minima in the overall potential [17].

3 Calculation of the rough magnetic field created by a distorted current flow in a wire

In this section, we present a general calculation of the extra magnetic field due to distortions in the current flow creating the trapping potential. By $\mathbf{j}$ we denote the current density that characterizes the distortion in the current flow. The total current density $\mathbf{J}$ is equal to the sum of $\mathbf{j}$ and the undisturbed flow $j_0\,\mathbf{e}_z$. As the longitudinal potential seen by the atoms is proportional to the z component of the magnetic field, we restrict our calculation to this component. We thus have to determine the x and y component of the vector potential $\mathbf{A}$ from which the magnetic field derives. In the following, we consider the Fourier transform of all the quantities of interest along the z axis which we define by

$$A_{l,k}(x,y) = \frac{1}{\sqrt{2\,\pi\,L}} \int A_l(x,y,z)\, e^{-i\,k\,z}\; dz \;, \qquad (1)$$

where we have used the vector potential as an example and l stands for x or y, L being the length of the wire. We choose this definition so that the power spectral density of a quantity coincides with the mean square of its Fourier transform :

$$\frac{1}{2\pi} \int e^{i\,k\,z}\; \langle A_l(z)\, A_l(0)\rangle\; dz = \langle |A_{l,k}|^2 \rangle \;. \qquad (2)$$

The vector potential satisfies a Poisson equation with a source term being proportional to the current density in the wire. Thus the Fourier component $A_{l,k}$ satisfies the following time independent heat equation

$$\left(\frac{\partial}{\partial x^2} + \frac{\partial}{\partial y^2}\right) A_{l,k} - k^2\, A_{l,k} = -\mu_0\, j_{l,k} \;. \qquad (3)$$

where j_l is one component of the current density $\mathbf{j}$. In the following, we use cylindrical coordinates defined by $x = r\,\cos(\varphi)$ and $y = r\,\sin(\varphi)$. Outside the wire, the right hand side of equation (3) is zero. The solution of this 2D heat equation without source term can be expanded in a basis of functions with a given "angular momentum"

n, the radial dependence of the solution being therefore a linear combination of modified Bessel functions of the first kind I_n and of the second kind K_n. Thus expanding $A_{l,k}$ on this basis, we obtain the following linear combination for the vector potential

$$A_{l,k}(r,\varphi) = \sum_{n=-\infty}^{n=\infty} c_{l_n}(k)\; e^{i\,n\,\varphi}\; K_n(k\,r)\;. \qquad (4)$$

We retain only the modified Bessel functions of the second kind, since the potential has to go to zero as r goes to infinity. The $c_{l_n}(k)$ coefficients are imposed by equation (3), and can be determined using the Green function of the 2D heat equation [21]. We obtain

$$c_{l_n}(k) = -\frac{\mu_0}{2\pi}\iint I_n(k\,r)\; e^{-i\,n\,\varphi}\; j_{l,k}(\varphi,r)\; r\,dr\,d\varphi\;. \qquad (5)$$

Taking the curl of the vector potential and using the relations $K_n' = -(K_{n-1}+K_{n+1})/2$ and $2\,n\,K_n(u)/u = -K_{n-1}+K_{n+1}$, we obtain the z component of the magnetic field from equation (4)

$$\begin{aligned} B_{z,k} = &-\frac{k}{2}\sum_{n=-\infty}^{\infty}[c_{y_{n-1}}(k)+c_{y_{n+1}}(k)]K_n(k\,r)e^{i\,n\,\varphi} \\ &-i\,\frac{k}{2}\sum_{n=-\infty}^{\infty}[c_{x_{n-1}}(k)-c_{x_{n+1}}(k)]K_n(k\,r)e^{i\,n\,\varphi}\;. \end{aligned} \qquad (6)$$

This expression is valid only for r larger than r_0, the radius of the cylinder that just encloses the wire. At a given distance x from the wire, we expect that only fluctuations with wavelengths larger or comparable to x contribute to the magnetic field, since fluctuations with shorter wavelengths average to zero. Therefore we can simplify expression (6) assuming we calculate the magnetic field above the center of the wire ($\varphi = 0$) for x much larger than r_0. The argument of I_n in equation (5) is very small in the domain of integration and we can make the approximation $I_n(k\,r) \simeq (k\,r)^n/(2^n\,n!)$. This shows that the c_{l_n} coefficients decrease rapidly with n. Keeping only the dominant term of the series in equation (6), we obtain

$$B_{z,k}(x) \simeq -\frac{c_{y_0}(k)}{k} \times \left[k^2\,K_1(k\,x)\right]\;. \qquad (7)$$

We will see in the next section that the first factor of this expression, characterizing the distortion flow, is proportional to the power spectral density of the wire corrugation. The second factor peaks at $k \simeq 1.3/x$ justifying the expansion. Fluctuations with a frequency much smaller or much larger than $1/x$ are filtered out and do not contribute. As we approach the wire, more and more terms have to be added in the series of equation (6) to compute the magnetic field. We emphasize that the expressions derived in equations (6) and (7) are general for any distorted current flow that may arise from bulk inhomogeneities or edge and surface corrugations.

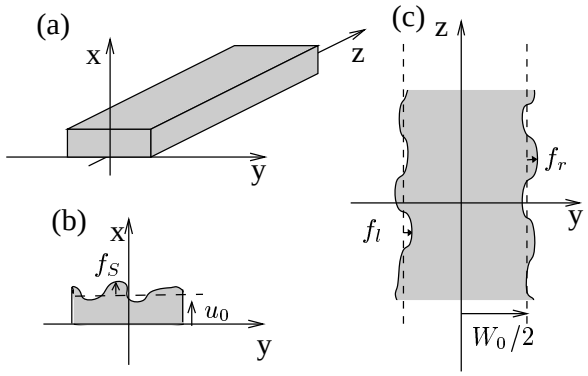

Fig. 1. Rectangular wire considered in this paper. The edge roughness and the top surface roughness are illustrated in (c) and (b) respectively.

4 Calculation of the distorted current flow in a corrugated wire

We now turn to the calculation of the distortion in the current flow due to wire edge and surface corrugations in order to determine the associated c_{l_n} coefficients. We suppose the wire has a rectangular cross section of width W_0 and height u_0 as shown on figure (1). Let us first concentrate on the effect of corrugations of the wire edges, which denote the borders perpendicular to the substrate. Figure (2) shows that, in our samples, these fluctuations are almost independent of the direction x both for wires deposited by electrodeposition and by evaporation. We believe this result to be general for wires fabricated by a lithographic process, since any defect in the mask or in the photoresist is projected all along the height of the wire during the fabrication process. Thus, in the following, the function $f_{r/l}$ that describes the deviation of the right (respectively left) wire edge from $\pm W_0/2$ is assumed to depend only on z.

Conservation of charge and Ohm's law give $\nabla\mathbf{J} = 0$ and $\mathbf{J} = -\chi\,\nabla V$ where χ is the electrical conductivity and V the electrostatic potential. We will make the approximation that χ is uniform inside the wire. In this case V satisfies the Laplace equation $\Delta V = 0$. As we are interested in deviations from the mean current density $j_0 = I/(u_0\,W_0)$, we introduce the electric potential $v = V - j_0\,z/\chi$ which is equal to zero in the absence of deviations. From what we have said above, v only depends on y and z and satisfies the 2D Laplace equation. The boundary conditions for the current density on the wire edge impose the current to be parallel to the wire edge. Thus v satisfies

$$\begin{aligned} \frac{df_{r/l}}{dz}(z) \times \left[j_0 - \chi\,\frac{\partial v}{\partial z}(y = \pm W_0/2 + f_{r/l}, z)\right] = \\ -\chi\frac{\partial v}{\partial y}(y = \pm W_0/2 + f_{r/l}, z)\;. \end{aligned} \qquad (8)$$

In the following we assume the amplitude of $f_{r/l}$ to be small enough so we can make an expansion to first order in $f_{r/l}$ of both terms. We then obtain a linear relation

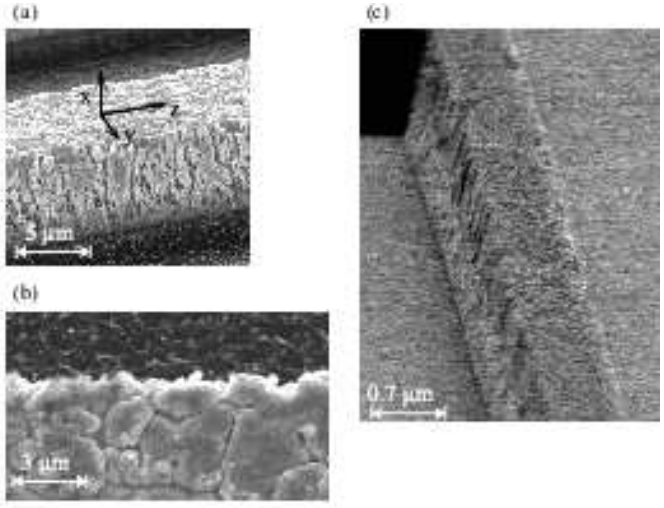

Fig. 2. Scanning electron microscope images of micro fabricated wires. Side view (a) and top view (b): electroplated gold wire of width 50 μm and height 4.5 μm fabricated using optical lithography. Side view (c): evaporated gold wire of width and height 0.7 μm fabricated using electron beam lithography.

between $v(\pm W_0/2, z)$ and $f_{r/l}(z)$ which in Fourier space can be written as

$$i\,k\,j_0\,f_{r/l,k} = -\chi\,\frac{\partial v_k}{\partial y}(y = \pm W_0/2)\ . \tag{9}$$

The potential v satisfies the 2D Laplace equation, so the k component $v_k(y)$ is a linear combination of $e^{+k\,y}$ and $e^{-k\,y}$. The two coefficients are imposed by the two boundary conditions of equation (9). To complete the calculation of these two coefficients, we introduce the symmetric component $f^+ = (f_r + f_l)/2$ and antisymmetric component $f^- = (f_r - f_l)/2$ of the wire edge fluctuations. Going back to the current density, we obtain

$$j_{y,k} = i\,k\,j_0\left(\frac{\cosh(k\,y)}{\cosh(k\,W_0/2)}f_k^+ + \frac{\sinh(k\,y)}{\sinh(k\,W_0/2)}f_k^-\right). \tag{10}$$

We note that the symmetric part (first term) of the current deviation is maximal near the wire edges for components with a wave vector large compared to $1/W_0$. On the other hand, the components with a small wave vector are constant over the width of the wire.

We now turn to the calculation of the current distortions due to surface corrugation. We assume the bottom surface to be flat, since the wire is supposed to be fabricated on a flat substrate. We denote by f_S the fluctuations of the height of the wire from its mean value u_0 (see figure (1)). We follow the same procedure as for the calculation of the effect of the wire edge fluctuations. Now v is the electrical potential associated with the current density j due to the surface corrugation. It depends on x, y and z and satisfies the 3D Laplace equation. To first order in f_S, the boundary conditions of a current tangent to the surface of the wire are

$$\begin{cases} \chi\dfrac{\partial v}{\partial x}(x = u_0, y, z) + j_0\dfrac{\partial f_S}{\partial z}(z) = 0 \\ \chi\dfrac{\partial v}{\partial x}(x = 0, y, z) = 0\ . \end{cases} \tag{11}$$

and

$$\frac{\partial v}{\partial y}(x, y = \pm W_0/2, z) = 0. \tag{12}$$

Symmetry arguments show that only the part of $f_S(y, z)$ which is odd in y contributes to the magnetic field along z in the plane $y = 0$. An even component of f_S produces currents which are symmetric under inversion with respect to the plane $y = 0$. Therefore, they cannot contribute to B_z in this plane. Thus, only the Fourier components

$$f_{S_{k,m}}(x) = \iint \frac{dy\,dz}{\pi\sqrt{2L\,W_0}}\ e^{-ikz}\sin(2m\pi y/W_0)\ f(y, z) \tag{13}$$

contribute. We choose this definition of the Fourier component $f_{S_{k,m}}$ so that $\langle|f_{S_{k,m}}|^2\rangle$ is equal to the 2-dimensional spectral density of f_S. To obtain the electric potential produced by a given component $f_{S_{k,m}}$ we use the expansion

$$\sin(2m\pi y/W_0) = \sum_{p=0}^{\infty}\gamma_{m,p}\sin((2p+1)\pi y/W_0), \tag{14}$$

where

$$\gamma_{m,p} = \frac{-8m}{\pi}\frac{(-1)^{m+p}}{(2(m+p)+1)(2(p-m)+1)}, \tag{15}$$

valid for $y \in [-W_0/2, W_0/2]$. Each p Fourier component induces an electrical potential $v_{k,m,p}$ and, since v satisfies the Laplace equation, $v_{k,m,p}(x)$ is a linear combination of $e^{+\nu_p x}$ and $e^{-\nu_p x}$ where $\nu_p = \sqrt{k^2 + ((2p+1)\,\pi/W_0)^2}$. The boundary conditions on the surfaces $x = 0$ and $x = u_0$ determine the coefficients and we obtain

$$-\chi\,v_{k,m,p} = i\,k\,j_0\,f_{S_{k,m}}\gamma_{m,p}\frac{\cosh(\nu_p x)}{\sinh(\nu_p u_0)}\frac{1}{\nu_p}\sin((2p+1)\pi y/W_0). \tag{16}$$

With the choice of the expansion (14), the boundary conditions on $y = \pm W_0/2$ are satisfied by each term. Finally, we obtain the current density distribution

$$\begin{cases} j_{x_{k,m}}(x, y) = 2ikf_{S_{k,m}}j_0\sqrt{\frac{\pi}{W_0}} \\ \qquad \displaystyle\sum_{p=0}^{\infty}\left(\gamma_{m,p}\frac{\sinh(\nu_p x)}{\sinh(\nu_p u_0)}\sin((2p+1)\pi y/W_0)\right) \\ j_{y_{k,m}}(x, y) = 2ikf_{S_{k,m}}j_0\sqrt{\frac{\pi}{W_0}} \\ \qquad \displaystyle\sum_{p=0}^{\infty}\left(\gamma_{m,p}\frac{\cosh(\nu_p x)}{\sinh(\nu_p u_0)}\frac{(2p+1)\pi}{\nu_p W_0}\cos((2p+1)\pi y/W_0)\right) \end{cases} \tag{17}$$

The Fourier component j_{l_k} is obtained by summing the previous expressions for $m = 1, \ldots, \infty$.

5 Rough potential of a ribbon shaped wire

In this section, we combine the results of the two previous sections to compute the z component of the rough magnetic field in the specific case of a flat rectangular wire ($u_0 \ll W_0$). This simplification enables us to obtain analytical results for a system that is widely used in experiments [1,2,3,5,7,18].

We do the calculation on the x axis for $x > W_0/2$. Since the wire is considered as flat, we replace the volume current density $\mathbf{j}$ by a surface current density $\sigma = \int \mathbf{j}\, dx$. Then we can rewrite the c_{l_n} coefficients as

$$c_{l_n}(k) = -\frac{\mu_0}{2\pi}(-i)^n \int_0^{W_0/2} dy I_n(ky)[\sigma_{l,k}(y)+(-1)^n\sigma_{l,k}(-y)] \; . \tag{18}$$

We will first study the effect of wire edge fluctuations and give universal behaviors for the magnetic field roughness. We will then concentrate on the effect of the top surface roughness. We will compare the relative importance of the two effects and point out important consequences for the design of micro wires.

5.1 Effect of wire edge roughness

Let us first study the effect of wire edge fluctuations. Here we derive the same results as [19] in a different way. The distorted current flow has no component along the x axis. The expression of the rough magnetic field is then given by the first sum of equation (6). Taking $\varphi = 0$, we can rearrange this sum using the equalities $K_n(kr) = K_{-n}(kr)$ and $c_{y_{-n}} = (-1)^n c_{y_n}$ (see equation (18)), we then obtain

$$B_{z,k} = -k \sum_{n=0}^{\infty} (c_{y_{2n}}(k) + c_{y_{2n+2}}(k)) K_{2n+1}(kr). \tag{19}$$

Since only the c_{y_n} with even n contribute, we see from equation (18) that only the symmetric part of the current density participates to the magnetic field. This is what we expect from a simple symmetry argument. For the $c_{y_{2n}}$ coefficients we obtain

$$c_{y_{2n}} = (-1)^{n+1} \frac{\mu_0 I}{\pi W_0}\, i\, k\, f_k^+ \times \int_0^{W_0/2} I_{2n}(k\,y) \frac{\cosh(k\,y)}{\cosh(k\,W_0/2)}\, dy \tag{20}$$

As pointed out in the previous section, the sum over the angular momenta n in equation (19) converges rapidly with n if $x \gg W_0$. More precisely, the dominant term proportional to $K_1(k\,x)$ gives the correct result within 10% as soon as $x > 1.5\,W_0$. As x approaches 0, more and more terms contribute, and for $x = W_0/2$, 20 terms have to be taken into account to reach the same accuracy.

We now derive the response function of the magnetic field to the wire edge fluctuation which we define as $R(k,x) = |B_{z,k}/f_k^+|^2$. As we already noticed in the previous section, far away from the wire ($x \gg W_0$), only wave vectors $k \ll 1/W_0$ are relevant. Then we can approximate the integral in equation (20) by expanding the integrand to zeroth order in $k\,y$. Keeping the dominant term in the series that defines the magnetic field, we obtain the following expression for the response function

$$R(k,x) \simeq \frac{(\mu_0 I)^2}{4\pi^2 x^4} (k\,x)^4 K_1^2(k\,x) \; . \tag{21}$$

For a given height x, as k increases, this function increases from zero as k^2, peaks at $k = 1.3/x$ and finally tends exponentially to zero. This behavior can be understood as follows. At low wave vectors, the angle between the direction of the distorted current flow and the z axis tends to zero, thus the contribution of these components becomes negligible. At high wave vectors, fluctuations with a wave length shorter than the distance to the wire average to zero.

To check the validity of equation (21), we plot the dimensionless function $R(k,x)/[(\mu_0 I)^2/(4\pi^2 x^4)]$ for different ratios x/W_0 in figure (3). The limit function corresponds to a configuration where the distorted current flow is concentrated on the line $x = y = 0$. For a smaller distance from the wire, the finite width of the wire becomes important and $R(k,x)$ differs from the expression (21). The amplitude is smaller and the peak is shifted to a lower frequency. These effects are due to the fact that as x decreases, the distance to the borders of the wire decreases less rapidly than the distance to the central part of the wire because of the finite width of the wire. Furthermore, because corrugations of high wave vector produce a current density localized near the wire border, their decrease in amplitude is more pronounced.

Assuming a white power spectrum of the wire edge corrugations with a spectral density J_e^+, we can integrate the equation (21) over the whole spectral range. We then find the following scaling law for the rms fluctuations of B_z with the atom-wire distance x:

$$\langle B_z^2 \rangle = J_e^+ \frac{(\mu_0 I)^2}{x^5} \times 0.044 \; . \tag{22}$$

This expression is valid for $x \gg W_0$, the numerical factor has been found by a numerical integration of equation (21). Figure (4) shows that this expression is valid within 10% as soon as $x > 2W_0$. For smaller distances x, the fluctuations of magnetic field increase more slowly and tends to a constant. Note that here J_e^+ is the spectral density of f^+. For edges with independent fluctuations, $J_e^+ = J_e/2$ where J_e is the spectral density of each wire edge. The asymptotic behavior of $\langle B_z^2 \rangle$ was first derived in [19].

5.2 Effect of top surface corrugation

We now consider the effect of corrugations of the top surface of the wire. As shown in equation (17), it induces both a current along the x and y direction. The surface current densities obtained by integration over x have remarkably simple forms. We find

$$\sigma_{y_{k,m}} = \sigma^{(1)}_{y_{k,m}} + \sigma^{(2)}_{y_{k,m}} \tag{23}$$

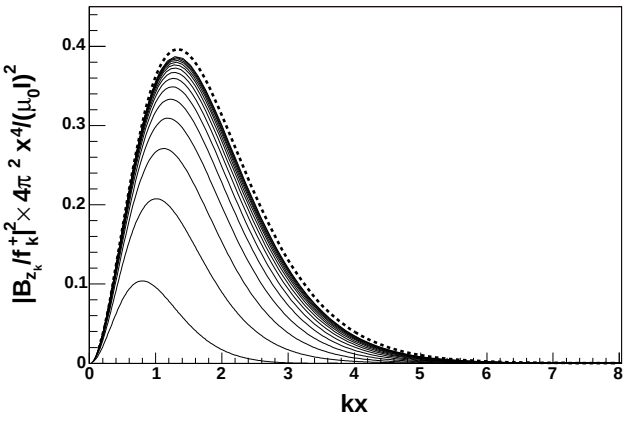

Fig. 3. Response function relating the magnetic field roughness $|B_{z_k}|^2$ to the wire edge fluctuations $|f_k^+|^2$ (see equation (21)). Plotted is the dimensionless quantity $|B_{z_k}/f_k^+|^2 \times 4\pi^2 x^4/(\mu_0 I)^2$ as a function of $k\,x$ where x is the height above the wire. The different curves correspond to different ratios x/W_0 going from 0.5 to 4.7 in steps of 0.3. Small values of x/W_0 correspond to lower curves. The curve corresponding to the limit given by equation (21) is also shown (dashed line).

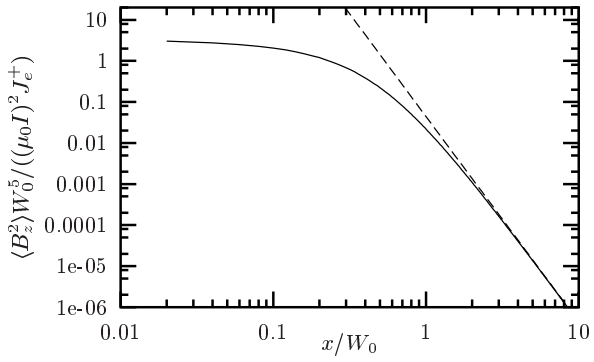

Fig. 4. Magnetic field fluctuations $\langle B_z^2\rangle$ as a function of the height above the wire. Plotted is the dimensionless quantity $\langle B_z^2\rangle\, W_0^5/((\mu_0 I)^2 J_e^+)$, where $\langle B_z^2\rangle$ is the magnetic field roughness and J_e is the spectral density of the wire edges assumed to be white, as a function of x/W_0 where x is the height above the the wire. Dashed line: $1/x^5$ law given by equation (22).

where

$$\begin{cases} \sigma^{(1)}_{y_{k,m}} = 2ikf_{S_{k,m}} j_0 \sqrt{\frac{\pi}{W_0}} \frac{2\pi m}{\kappa^2 W_0} \cos(\frac{2\pi m y}{W_0}) \\ \sigma^{(2)}_{y_{k,m}} = -2ikf_{S_{k,m}} j_0 \sqrt{\frac{\pi}{W_0}} \frac{2\pi m}{\kappa^2 W_0} (-1)^m \frac{\cosh(ky)}{\cosh(kW_0/2)} \end{cases} \tag{24}$$

and $\kappa = \sqrt{k^2 + (2m\pi/W_0)^2}$. In the calculation of $\sigma_{x_{k,m}}$ the summation over p is not analytical. However, as we consider wires with $u_0 \ll W_0$, one can make the approximation $(\cosh(\nu_p u_0) - 1)/\sinh(\nu_p u_0) \simeq \nu_p u_0$. We then obtain

$$\sigma_{x_{k,m}} = ikf_{S_{k,m}} j_0 \sqrt{\frac{\pi}{W_0}} u_0 \sin(2m\pi y/W_0). \tag{25}$$

Comparing equation (25) and equation (24), we see that the current density along x is much smaller than the current density along y as long as Fourier components $\kappa \ll 1/u_0$ are considered. Within our flat wire approximation, where only distances from the wire $x \gg u_0$ are considered, this is always the case. In the following we therefore only consider the effect of the current density along y. For $x \geq W_0/2$, the rough magnetic field is then given by equation (19).

Assuming a white power spectrum for the surface corrugation of spectral density J_S, we now derive some properties of the rough magnetic field. For distances above the wire $x \gg W_0$, only k components much smaller than $1/W_0$ are relevant. Then, as we have already shown, the c_{l_n} coefficients decrease rapidly with n and the dominant contribution is given by c_{y_0}. To lowest order in ky, c_{y_0} is proportional to the total current $\int_{-W_0/2}^{W_0/2} \sigma_y(y)dy$. Thus, the only contribution comes from $\sigma^{(2)}_{y_{k,m}}$. Then, calculations similar to those presented in the previous section show that the contribution to $\langle B_z^2\rangle$ of the Fourier component m of f_{S_k} is

$$\langle B^2_{z,m}\rangle = J_s \frac{W_0}{\pi u_0^2} \frac{1}{m^2} \frac{(\mu_0 I)^2}{x^5} \times 0.044 \tag{26}$$

where J_s is the 2-dimensional spectral density of f_S. As expected it decreases with m as the contribution of rapidly oscillating terms averages to zero for large distances $x \gg W_0$. Computing the sum over $m > 0$ gives the scaling law for the rms fluctuation of B_z due to surface corrugation with atom-wire distance x:

$$\langle B_z^2\rangle = J_s \frac{W_0}{u_0^2} \frac{\pi}{6} \frac{(\mu_0 I)^2}{x^5} \times 0.044 \tag{27}$$

In figure (5) this expression is compared to numerical calculations based on equation (24). The terms $\sigma^{(2)}_{y_{k,m}}$ contribute at least 90% of $\langle B_z^2\rangle$ as soon as $x > W_0$.

Comparing edge and surface corrugation, we see that for large distances, both effects scale in the same way (see equations (22) and (27)). However, at short distances from the wire, the amplitude of the magnetic field roughness produced by surface corrugation does not saturate. Indeed, although the contribution of $\sigma^{(2)}_{y_{k,m}}$ saturates in the same way as the effect of wire edge fluctuations, the contribution of $\sigma^{(1)}_{y_{k,m}}$ to the current density diverges as one gets closer to the wire. Thus at small distances from the wire, we expect surface roughness to become the dominant source of magnetic field fluctuations.

5.3 Consequences for micro wire traps

The scaling laws (22) and (27) are of major importance as they impose strong constrains in the use of micro traps. As mentioned in section 2, high magnetic field gradients are achieved with small wires and short distances. But as the distance to the wire decreases, the roughness in the magnetic trapping potential increases. Imposing a maximal roughness $\Delta B_{\max}$ tolerable in an experiment there-

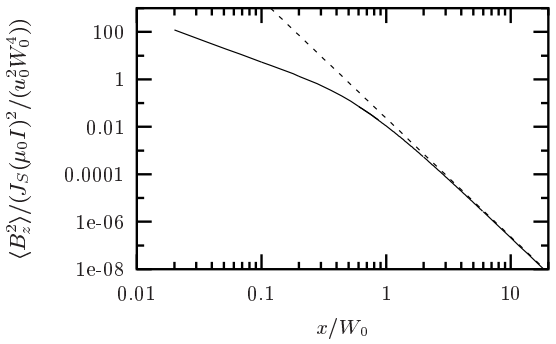

Fig. 5. Longitudinal magnetic field fluctuations $\langle B_z^2\rangle$ produced by white noise top surface wire roughness as a function of x/W_0. Plotted is the dimensionless quantity $\langle B_z^2\rangle/(J_S(\mu_0 I)^2/(u_0^2 W_0^4))$. The dashed lines represents equation (27).

fore directly determines the maximal transverse gradient accessible with a given realization of a micro wire.

More precisely, as mentioned in section 2, the maximal current in a micro wire is limited by heat dissipation: $I_{\max} = \kappa W_0 u_0^{1/2}$ [20]. To analyze the scaling of the system, we consider the trap center at a distance comparable to the wire width $x \simeq W_0$ and a wire height u_0 small and constant. For a given fabrication technology, we expect the wire roughness to be independent of the wire dimensions W_0 and u_0 and we assume white noise spectral densities J_e and J_S for the edge and top surface corrugations. Using the above expressions for x and I and equations (22) and (27), we obtain the following scaling laws

$$\begin{aligned}\langle B^2_{\rm edge}\rangle &= \tfrac{J_e \mu_0^2 \kappa^2 u_0}{W_0^3}\\ \langle B^2_{\rm surf}\rangle &= \tfrac{\pi}{6}\tfrac{J_S \mu_0^2 \kappa^2}{W_0^2 u_0}\end{aligned} \tag{28}$$

for the magnetic field fluctuations induced by the edge and the surface roughness respectively. Imposing magnetic field fluctuations smaller than $\Delta B_{\max}$ determines a minimal wire width $W_{0,\min}$ and the maximal transverse gradient $\nabla B_{\max}$. If the potential roughness is dominated by effects due to wire edge corrugation, we find:

$$\begin{aligned}W_{0,\min} &= \left(\tfrac{J_e \mu_0^2 \kappa^2 u_0 \times 0.044}{\Delta B^2_{\max}}\right)^{1/3}\\ \nabla B_{\max} &= \tfrac{1}{2\pi}\left(\tfrac{\mu_0 \kappa \sqrt{u_0} \Delta B^2_{\max}}{J_e \times 0.044}\right)^{1/3}.\end{aligned} \tag{29}$$

For a potential roughness dominated by effects due to wire top surface corrugation, we find:

$$\begin{aligned}W_{0,\min} &= \left(\tfrac{\pi}{6}\tfrac{J_S \mu_0^2 \kappa^2 \times 0.044}{\Delta B^2_{\max} u_0}\right)^{1/2}\\ \nabla B_{\max} &= \tfrac{1}{2\pi}\left(\tfrac{u_0 \Delta B_{\max}}{J_S \frac{\pi}{6} \times 0.044}\right)^{1/2}.\end{aligned} \tag{30}$$

As will be described in the following section, a micro wire fabricated by electroplating presents an edge roughness of $J_e \simeq 0.1\,\mu\mathrm{m}^3$. Assuming a wire without top surface roughness, a wire height of $u_0 = 5\,\mu$m, a typical $\kappa = 3 \times 10^7\,\mathrm{A.m}^{-3/2}$ and imposing a maximal potential roughness of $\Delta B_{\max} = 100\,$mG, the wire width is limited to $W_{0,\min} \simeq 70\,\mu$m, the maximal gradient will be $\Delta B_{\max} \simeq 2\,\mathrm{T/cm}$.

6 Probing the rough magnetic potential with cold atoms

In a previous letter [17], we described measurements of the magnetic field roughness produced by a current carrying micro fabricated wire. The basic idea is to use the fact that the longitudinal density $n(z)$ of atoms along the wire, is related to the longitudinal potential seen by the atoms through a Boltzmann factor:

$$n(z) \propto e^{-V(z)/k_{\rm B}T}. \tag{31}$$

As discussed in section 2, the potential $V(z)$ is proportional to the z-component of the magnetic field a the center of the trapping potential. Our typical thermal energy, $1\,\mu$K, corresponds to a magnetic field of $15\,\mu$G for a ^{87}Rb atom in the $F = 2, m_F = 2$ state. Since longitudinal density variations of order 10% are easily visible in our experiment, we are sensitive to variations in the magnetic field at the mG level.

The micro wire we used to create the magnetic potential is a $50\,\mu$m wide electroplated gold wire of $4.5\,\mu$m height. The process of micro fabrication is the following: a silicon wafer is first covered by a 200 nm silicon dioxide layer using thermal oxidation. Next, seed layers of titanium (20 nm) and gold (200 nm) are evaporated. The wire pattern is imprinted on a $6\,\mu$m thick photoresist using optical UV lithography. Gold is electroplated between the resist walls using the first gold layer as an electrode. The photoresist is then removed, as well as the first gold and titanium layers. Finally the wire is covered with a $10\,\mu$m layer of BCB resin and a 200 nm thick layer of evaporated gold. The gold surface acts as a mirror for a magneto-optical trap. The procedure for deducing the potential roughness from images of the atomic cloud is complex and we refer the reader to [17].

Figure (6) shows the measured longitudinal potential for various distances above the wire. We also show the power spectral density of these potentials in figure (7). A region of 1.6 mm along the wire is explored by the atoms. To estimate the power spectral density of the potential roughness we divide the total window in three smaller windows overlapping by 50% [22]. In each window, the fourier transform of the potential is computed after multiplication with a Hamming window and the estimate of the spectral density is the average of the square of the Fourier transforms.

In figure (7), a flat plateau is visible at the highest wave vectors (*e.g.* $k > 0.07\,\mu\mathrm{m}^{-1}$ at 46 μm and $k > 0.04\,\mu\mathrm{m}^{-1}$ at 80 μm). The level of this plateau depends on experimental parameters such as the temperature and density of the atom cloud. On the other hand the spectral density at low wave vectors, *i.e.* in the region where it rises above the

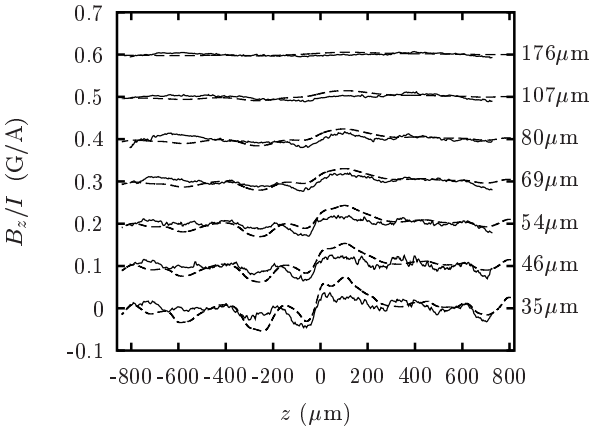

Fig. 6. Rough magnetic field $B_z(z)$ normalized to the current in the micro wire. Solid lines: magnetic field measured using cold atomic clouds. Dashed lines: magnetic field calculated from the measured corrugation of the edges of the wire. The different curves have been vertically shifted by 0.1 G/A from each other and heights above the wire are indicated on the right.

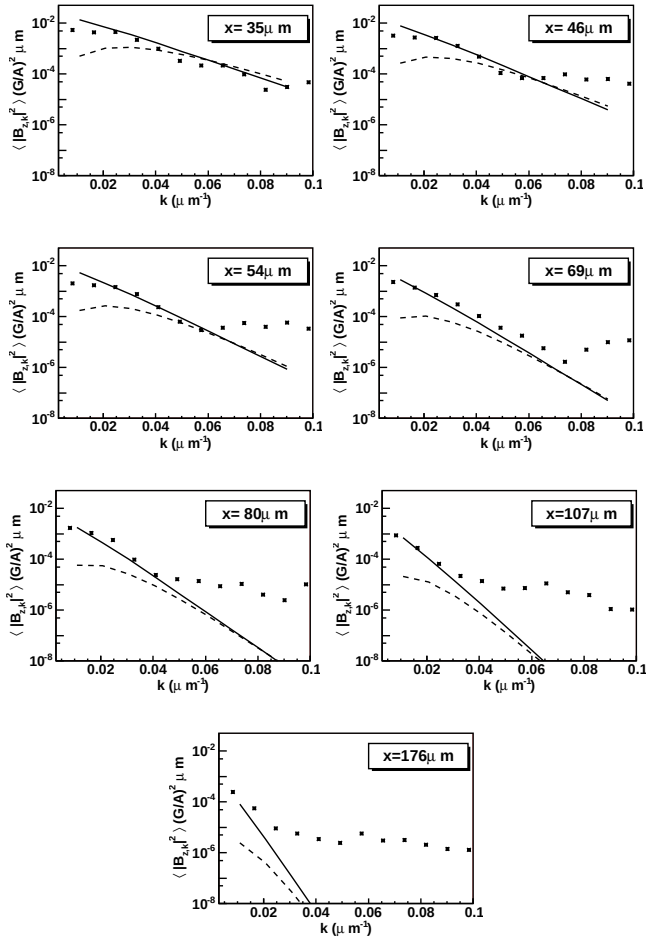

Fig. 7. Spectral density of the magnetic field roughness for different heights above the wire. The points represent experimental data. The curves result from the calculations detailed in the text. Solid curves: expected noise due to wire edge roughness. We used the power law fit to the spectral density of the wire border fluctuations. Dashed curves: expected noise due to top surface roughness.

plateau, is independent of these parameters. This observation leads us to conclude that while the low wave vector part of the spectrum corresponds to a potential seen by the atoms, the plateau at high wave vectors is due to instrumental noise in our imaging system, such as fringes. We expect it to vary in a complex way with temperature and atom density. Qualitatively, smaller atom-wire distances, which are analyzed with higher temperature clouds, should result in higher plateaus. This tendency is indeed observed in figure (7).

To measure the wire corrugations, we removed the atom chip from vacuum and etched off the gold mirror and the BCB layer. We analyzed the bare wire with scanning electron microscopy (SEM) and with atomic force microscopy (AFM) techniques. The function f describing the edge corrugation is extracted from SEM images such as (2b). Rms deviations of the edges are as small as 200 nm, and we use a $50\,\mu$m $\times$ $50\,\mu$m field of view in order to have a sufficient resolution. We use 66 overlapping images to reconstruct both wire edges over the whole wire length of 2.8 mm. We identify no correlation between the two edges. The spectral density obtained for $f^+ = (f_l + f_r)/2$ is plotted in figure (8). We see two structures in the spectrum: first, we observe fluctuations with a correlation length of $0.2\,\mu$m and 100 nm rms amplitude. It corresponds to the fluctuations seen on figure (2b) which are probably due to the electrodeposition process. Second, roughness with low wave vectors is present and raises significantly the power spectral density in the 0.01-0.1 μm^{-1} range. For the spectral range 0.01-1 μm^{-1}, the wire border fluctuations are well fitted by a power law $J = 3.2 \times 10^{-6} k^{-2.15} + 8.2 \times 10^{-4}\,\mu$m^3 as seen in figure (8). We use this expression to compute the spectra shown in figure (7). As we measured f over the whole region explored by the atoms, we can not only compare the spectral densities of the magnetic field roughness but we also can compare the direct shape of the magnetic field $B_z(z)$. This is done in figure (6) where the magnetic field, computed from f as described in the previous sections, is shown by dashed lines. We note that no adjustment has been applied to superimpose the two curves, the absolute position of the atoms with respect to the wire is known to the $3\,\mu$m resolution of our imaging system.

The corrugation of the top surface of the wire is measured using an AFM and the observed power spectral density is plotted in figure (9). The spectrum is flat for wave vectors smaller than $1\,\mu$m^{-1} with a value $J_S = 1.6 \times 10^{-3}\,\mu$m^4. Unfortunately, we were not able to obtain the spectrum for very long wave vectors. For purposes of calculation, we shall simply assume that the spectral density below $0.1\,\mu$m^{-1} has the same value as between 0.1 and $1\,\mu$m^{-1}. The results of this calculation is plotted figure (7) (dashed lines).

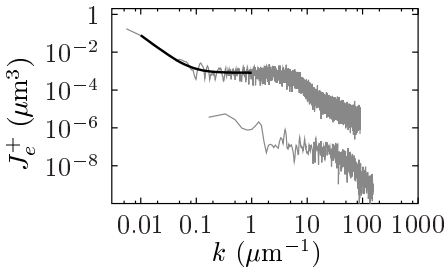

Fig. 8. Measured spectral density of the edge roughness of the electroplated wire (upper curve) and of the evaporated wire (lower curve). For the electroplated wire, the spectral density of $f^+ = (f_l + f_r)/2$ is plotted. For the electroplated wire, $J_f/2$ is plotted, where J_f is the spectral density of a single border of the wire, as expected for the spectral density of f^+ for independent wire border fluctuations. The thick line on the upper curve is a power law fit $J = ax^{-b} + c$ which gives $b = 2.19$.

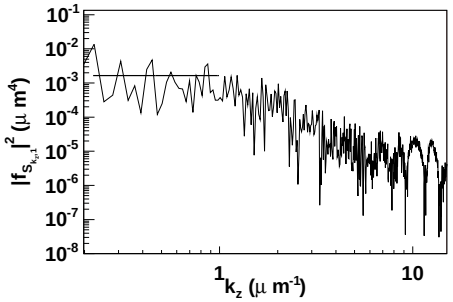

Fig. 9. Power spectral density of the wire top surface roughness measured with an AFM. We plot the spectral density corresponding to the transverse mode $m = 1$ ($k_y = 2\pi/W_0$) which is the first one to contribute to magnetic field roughness. The horizontal line indicates the mean value for k_z ranging from $0.2\,\mu\mathrm{m}^{-1}$ to $0.1\,\mu\mathrm{m}^{-1}$.

Our results indicate that the magnetic field roughness measured with cold atoms is explained by wire corrugation. At low wave vectors ($k < 0.04\,\mu\mathrm{m}^{-1}$), it seems that the magnetic field roughness is primarily due to edge corrugations. The good agreement between the observed field and the calculation shown in figure (6) are the strongest evidence for this conclusion. For wave vectors larger than about $0.5\,\mu\mathrm{m}^{-1}$, the corrugations of the top surface are expected to contribute as strongly as those of the edges. This wave vector regime however, is not being stringently tested by our data. Since we have no data on surface corrugation at wave vectors below $0.1\,\mu\mathrm{m}^{-1}$, it is possible that the contribution from this effect is larger than shown in figure (7). The atom data in the figure however, indicate that the surface effect is not the dominant one although given our signal-to-noise it could be of comparable magnitude.

7 Improved fabrication process for micro wires

The fabrication technology described above limits us to atom wire separations greater than several tens of microns if we want to obtain a reasonably smooth potential. In order to improve the quality of our wire, we turn to a different micro fabrication process: the wire structures are patterned onto an oxidized silicon wafer using electron beam lithography. We use gold evaporation and a standard lift-off technique to obtain 700 nm square cross section wires as shown in figure (2c).

We extract the wire border roughness from SEM images and the obtained power spectral density is plotted in figure (8) (lower curve). In the spectral range studied, the roughness is greatly reduced compared to the first fabrication process. This was expected as the grain size of evaporated gold is much smaller than of electroplated gold. Unfortunately, we do not have a quantitative measurement of the power spectral density in the 0.01-0.1 μm^{-1} range. Indeed, as we had to reduce the field of view to increase the resolution, it becomes very difficult to overlap hundreds of SEM pictures without adding spectral components due to stitching errors.

Gold evaporation produces surfaces of optical quality at visible light. Thus the roughness of the top surface of the evaporated wire is expected to be much smaller than that of an electroplated wire.

8 Conclusion

Our goal in this paper has been to give a more detailed description of the work which led to our conclusion that wire corrugations can account for the magnetic field roughness typically observed in atom chip experiments. We wish to emphasize in this paper that great care must be taken to characterize the roughness of a micro fabricated wire. The ratio of the rms roughness to the wavelength of the imperfections is below 10^{-4}. Thus a single microscope image cannot reveal the imperfections.

The model we use has already been suggested in reference [19]. Here we have given more details of the calculation as well as some physical arguments explaining the results. We have also extended the calculation to include the effects of corrugations of the top surface of the wire. The top surface corrugations become increasingly important as the distance to the wire decreases, while the effect due to wire edge roughness saturates.

The equations (22) and (27), giving the behavior of the magnetic field roughness due to edge and surface corrugation as a function of height, are important scaling laws that one should keep in mind in the design of atom chips. The requirements of small roughness and high transverse confinement impose a tradeoff in choosing a wire size for a given fabrication quality. We do not believe however that we are at the end of our progress in improving the fabrication technology [20]. Thus sub-micron scale atom chips continue to hold out much promise for the manipulation of ultra cold atoms.

We thank David Hermann for help in calculations. This work was supported by The E.U. under grant (IST-2001-38863 and MRTN-CT-2003-505032), as well as by the DGA (03.34.033).

References

1. W. Hänsel, P. Hommelhoff, T. W. Hänsch, and J. Reichel, Nature **413**, 498 (2001).
2. D. Cassettari *et al.*, Phys. Rev. Lett. **85**, 5483 (2000).
3. H. Ott *et al.*, Phys. Rev. Lett. **87**, 230401 (2001).
4. E.A. Hinds, C.J. Lukin, and M.G. Boshier, Phys. Rev. Lett. **86**, 1462 (2001).
5. A. E. Leanhardt *et al.*, Phys. Rev. Lett. **89**, 040401 (2002).
6. D. Müller *et al.*, Phys. Rev. Lett. **83**, 5194 (1999).
7. Y. Lin, I. Teper, C. Chin, and V. Vuletic, Phys. Rev. Lett. **92**, 050404 (2004).
8. R. Folman *et al.*, Adv. Atom. Mol. Opt. Phys. **48**, 263 (2002), and references therein.
9. T. Calarco *et al.*, Phys. Rev. A **61**, 022304 (2000).
10. C. Henkel, S. Pötting, and M. Wilkens, Appl. Phys. B **69**, 379 (1999).
11. C. Henkel and M. Wilkens, Europhys. Lett. **47**, 414 (1999).
12. M. P. A. Jones *et al.*, Phys. Rev. Lett. **91**, 80401 (2003).
13. D. Harber, J. McGuirk, J. Obrecht, and E. Cornell, J. Low Temp. Phys. **133**, 229 (2003).
14. J. Fortàgh *et al.*, Phys. Rev. A **66**, 41604 (2002).
15. S. Kraft *et al.*, J. Phys. B **35**, L469 (2002).
16. M. P. A. Jones *et al.*, J. Phys. B: At. Mol. Opt. Phys. **37**, L15 (2004).
17. J. Estève *et al.*, physics/0403020 (2004).
18. C. Vale *et al.*, cond-mat/0406015 (2004).
19. D.-W. Wang, M. Lukin, and E. Demler, Phys. Rev. Lett. **92**, 076802 (2004).
20. S. Groth *et al.*, cond-mat/0404141 (2004).
21. G. B. Arfken and H. J. Weber, *Mathematical methods for physicists (fourth edition)* (Academic Press, San Diego, California, 1995), p. 519.
22. P. D. Welch, IEEE Trans. Audio and Electroacoustics **AU-15**, 70 (1967).